catalysts

MDPI

Article

The Biomass of Pig-Blood-Derived Carbon as a Novel Electrode Material for Hydrogen Peroxide Electrochemical Sensing

Guolei Liu [1,†], Xue Li [2,†], Qing Wang [3], Kuizhao Sun [2], Chuping Lee [4], Yue Cao [3,*], Weimeng Si [3], Haoran Wei [5], Zhongfang Li [2] and Fagang Wang [3,*]

1 School of Resources and Environmental Engineering, Shandong University of Technology, Zibo 255000, China
2 School of Chemistry and Chemical Engineering, Shandong University of Technology, Zibo 255000, China
3 School of Material Science and Engineering, Shandong University of Technology, Zibo 255000, China
4 Department of Chemistry, Fu Jen Catholic University, New Taipei City 24205, Taiwan
5 Department of ECE, University of Texas at Dallas, Richardson, TX 75080, USA
* Correspondence: cao-yue@foxmail.com (Y.C.); a_gang@sdut.edu.cn (F.W.)
† These authors contributed equally to this work.

Abstract: In the work, a pig-blood-derived mesoporous carbon (BC) was prepared as a novel Fe-N-C material for the electrochemical sensor to detect hydrogen peroxide. Because of the unique nanostructure of Fe-BCs with rough surface structure, hierarchical pores, and high graphitization degree, the Fe-BCs, as a kind of advanced electrode material, exhibited remarkable performance in electrocatalysis. The sensor based on Fe-BCs exhibited an extra-long range from c and a detection limit of 0.046 μM (S/N = 3). The synthesis of low-cost, advanced carbon-based electrode materials from environmentally friendly pig blood for electrochemical sensor construction is a promising approach.

Keywords: electrochemical sensors; hydrogen peroxide detection; biomass carbon

Citation: Liu, G.; Li, X.; Wang, Q.; Sun, K.; Lee, C.; Cao, Y.; Si, W.; Wei, H.; Li, Z.; Wang, F. The Biomass of Pig-Blood-Derived Carbon as a Novel Electrode Material for Hydrogen Peroxide Electrochemical Sensing. *Catalysts* **2022**, *12*, 1438. https://doi.org/10.3390/catal12111438

Academic Editors: Dezhi Han, Wentai Wang and Ning Han

Received: 22 September 2022
Accepted: 4 November 2022
Published: 15 November 2022

1. Instruction

Hydrogen peroxide (H_2O_2) is a typical reactive oxygen species (ROS) and plays a key role in various normal biological processes and the food industry [1,2]. As an essential kind of intracellular signaling molecule, reactive oxygen species (ROS) are closely correlated with numerous cellular functions and play an essential role in cellular physiology, providing a reliable diagnosis of pathological conditions [3]. H_2O_2 is also a by-product of classical biochemical reactions catalyzed by enzymes such as glucose oxidase. Therefore, it is of great importance to develop accurate, rapid, and reliable methods for the detection of H_2O_2. The conventional methods used for the determination of hydrogen peroxide are mainly fluorescence analysis, chromatography, titration chemiluminescence, and spectrophotometric methods [4–6]. These processes are complex, expensive, and time-consuming to perform. In contrast, since H_2O_2 is an electroactive molecule, electrochemical detection is a simple, rapid, sensitive, and cost-effective detection strategy [7–9].

Biomass carbon materials are now one of the most popular research areas in electrochemistry, and their rich pore channels, large specific surface area, and high chemical resistance make the research mostly focused on the energy field [10]. Biomass carbon has a relatively stable three-dimensional structure [11–13]. Biomass carbon has a relatively stable three-dimensional structure. As a result, it can withstand a certain degree of mechanical, biological, and chemical attack [14–16]. The structure becomes more stable after chemical, thermochemical, or biological treatment to remove its easily degradable components. As a result of the removal of those easily degradable components, many channels and pores are formed in the resulting matrix [17–20]. The formation of cavities during degradation is not regular, and although the abundant channels and pore structures facilitate the exposure of active sites and adsorption of the target to be measured, the overly complex pore structures are not conducive to the mass transfer process during sensing, which in turn affects the

amplification of the electrochemical response signal [21–23]. The electrochemical response information is easily masked by significant charging and discharging processes, often to the detriment of sensor construction [24]. Nevertheless, the application of biomass carbon materials in sensing has its unique attraction in two points: the continuity of charge transfer channels and the highly rough surface properties. The continuous charge transfer channel can significantly reduce the charge transfer resistance, thus enabling signal amplification; the highly rough surface facilitates the increase in surface active sites, which also facilitates signal amplification [21,24–26]. Moreover, this rough structure is a reflection of the internal extension of the material itself to the surface, which has a high degree of controllability, uniformity, and microstructural stability.

At this stage, the common methods for preparing biomass carbon materials include pyrolysis, chemical vapor deposition (CVD), cyclic oxidation, mechanical activation, and combustion [27–30]. Biomass pyrolysis is commonly used to prepare activated carbon, and it is easy to obtain porous carbon materials with a high specific surface area. However, due to the complex structure of biomass, a large number of heteroatoms other than C, and the strong chemical bonds, the carbon atoms cannot be easily rearranged in an orderly and regular manner by pyrolysis alone, and it is not easy to obtain carbon nanomaterials with high crystallinity [31–34]. Pyrolytic biomass carbon generally possesses a complex pore structure that can significantly affect the mass transfer process, leading to its lesser application in electrochemical sensing and a few related reports [35]. Therefore, the design and preparation of high-performance heteroatom-doped 3D carbon materials by improving the biomass carbon pyrolysis process and using them for the construction of electrochemical sensors is of great significance in achieving efficient electrochemical detection of hydrogen peroxide.

In this work, Fe-N-S-C composites (Fe-BC) based on pig-blood precursors (blood carbon, BC) were prepared by high-temperature pyrolysis based on the highly controllable nature of pig blood. The pig-blood gel has the advantages of low cost and environmental friendliness and is an ideal material for the construction of biomass carbon materials. The highly rough nature of the surface facilitates the increase in surface active sites on the one hand and increases the H_2O_2 contact efficiency on the other hand, which facilitates the signal amplification. The Fe-BC/GCE (glassy carbon electrode) can be used to construct H_2O_2 sensors with high stability and excellent performance.

2. Result and Discussion

Figure 1A shows the SEM image of Fe-BC-300, from which it can be observed that there is no obvious pore structure on the surface of Fe-BC-300. As shown in Figure 1B, with the increase in the pyrolysis temperature to 600 °C, the biomass, such as proteins within the pig blood, started to decompose, and the pore structure began to appear from the middle of the material. It was observed that a large number of uniformly dispersed nanopores could be clearly observed on the surface of Fe-BC-900 (Figure 1C). Figure 1D SEM (after magnification by ten times) image of Fe-BC-900 can be observed that the pore size of the material is between 30–100 nm. A large number of pores can provide a more specific surface area and increase the contact opportunity between the catalyst and the material to be measured, improving the sensor performance [24]. When the relative pressure (P/P_0) is less than 0.1, the isotherms rise in a logarithmic shape, indicating the existence of a large number of micropores in Fe-BC-900. The porosity of the samples was further characterized using nitrogen adsorption and desorption, as shown in Figure S1. For Fe-BC-900, there are two inconspicuous hysteresis loops at $P/P_0 > 0.4$, which prove the presence of mesopores in both samples. The QSDFT pore size is displayed in Figure 1B. Note that the Fe-BC-900 hysteresis loop reveals a mesoporous structure with a pore-size distribution based on about 8 nm.

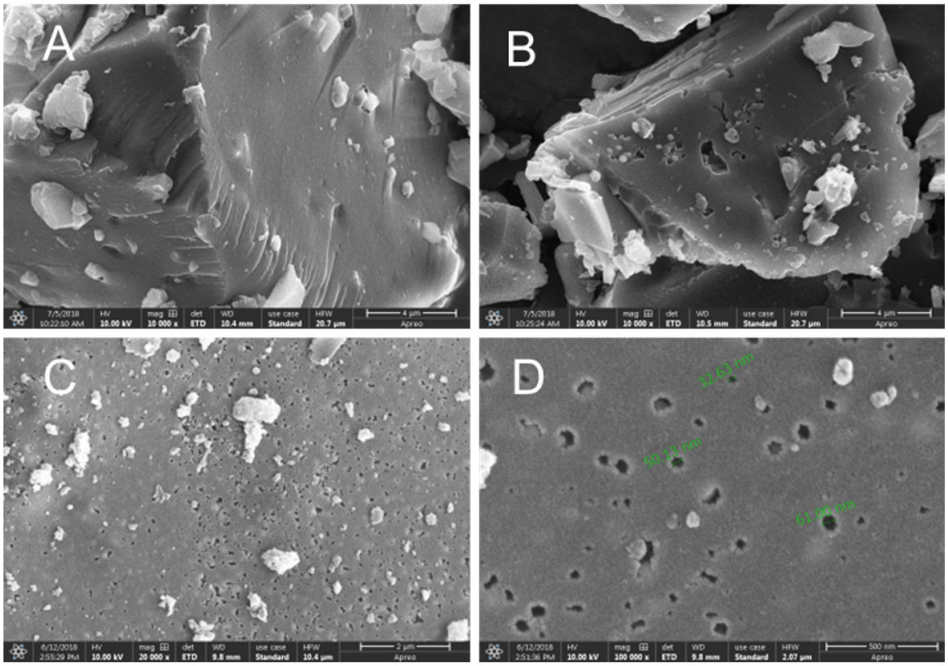

Figure 1. SEM images of Fe-BC-300 (**A**), SEM images of Fe-BC-600 (**B**), and SEM images of Fe-BC-900 (**C**,**D**).

The structures and morphologies of Fe-BC-300, Fe-BC-600, and Fe-BC-900 can be further observed by TEM images. The TEM of Fe-BC-300 is shown in Figure 2A,B, where the nano black particles are wrapped in the carbon layer, presumably due to the low pyrolysis temperature and the short pyrolysis time resulting in insufficient decomposition of the biomass to obtain the pore structure. When the pyrolysis temperature was increased to 600 °C, it can be observed that a microporous structure appeared on the surface of the material, and the material dispersion was also improved. Figure 2C shows the TEM of Fe-BC-900, and a more uniform pore structure can be clearly observed, which is the same as the SEM results. Figure 2E–H shows the EDS (Energy dispersive X-ray spectroscopy) energy spectra of Fe-BC-900 C element, N element, S element, and Fe element, from which it is seen that N element, S element, and Fe element are uniformly scattered within the carbon skeleton, indicating the successful synthesis of the doped material.

As shown in Figure 3, Raman spectroscopy was further used to investigate the degree of defects and graphitization of Fe-BC-900 composites. The Raman spectra show two peaks at approximately 1340 cm^{-1} and 1594 cm^{-1}, corresponding to the D and G bands, respectively. I_D/I_G can provide an indication of the number of structural defects and a quantitative metric of edge plane exposure. The calculated I_D/I_G of Fe-BC-900 is 0.89, which indicates that the high pyrolysis temperature is more favorable to the formation of graphitic crystalline structure, and the high graphitization is beneficial to improve the surface charge transport of the nano-catalyst, which can greatly improve the material sensitivity [36,37].

The electrochemical behavior of BC/GCE, Fe-BC-300/GCE, Fe-BC-600/GCE, and Fe-BC-900/GCE in KOH was studied using CV. Figure 4A shows the CV curves of different modified electrodes in 0.1 M KOH solution saturated with 100 mV s^{-1} N_2 at the scan rate. It can be observed from the figure that the capacitance current of each Fe-BC modified electrode increases with the increase in the pyrolysis temperature, which is due to the increase in BC graphitization with the increase in the pyrolysis temperature. In contrast to Fe-BC-900/GCE, BC-900/GC exhibits a larger background current, which may be due to the removal of iron from the material with surface impurities by hydrochloric acid, which improves the charge conduction.

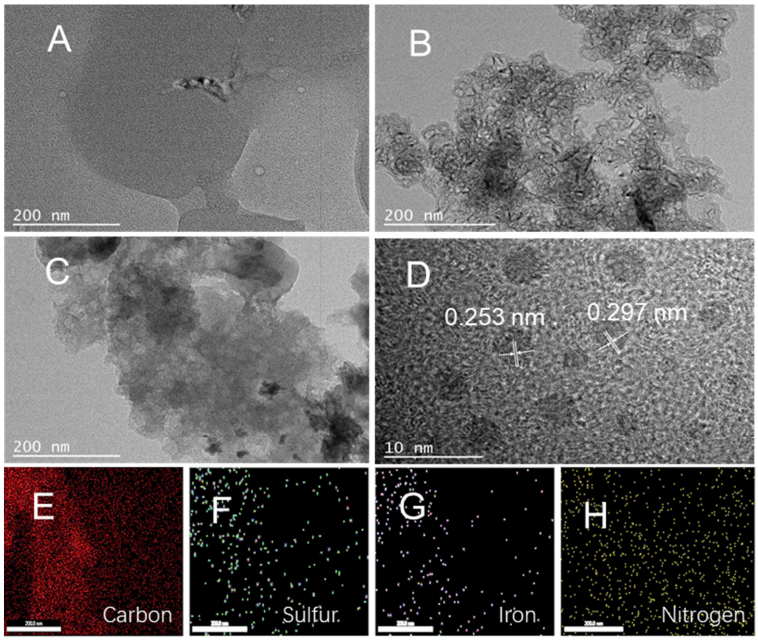

Figure 2. TEM image of PPY-H-CBN (**A**), Fe-BC-600 (**B**), and Fe-BC-900 (**C**); (**D**) HRTEM image of Fe-BC-900; (**E**–**H**) elemental mapping of C, S, Fe and N for Fe-BC-900.

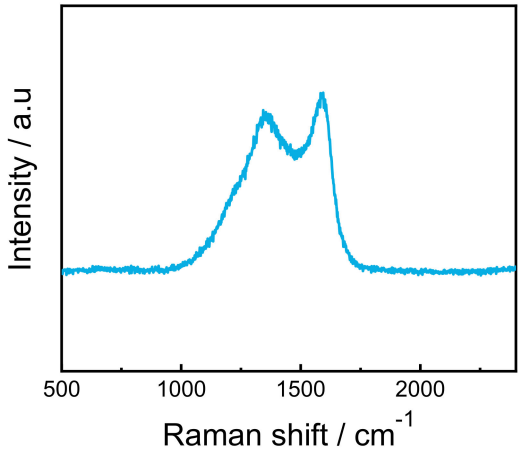

Figure 3. Raman spectra of Fe-BC-900.

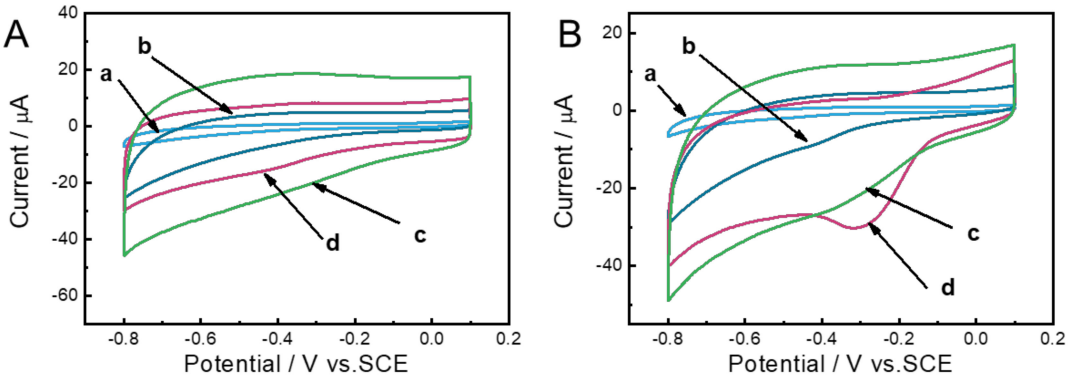

Figure 4. (**A**) CVs of the Fe-BC-300/GCE (a), Fe-BC-600/GCE (b), Fe-BC-900/GCE (c), and Fe-BC-900/GCE (d) in N_2-saturated 0.1 M KOH; (**B**) CVs of the Fe-BC-300/GCE (a), Fe-BC-600/GCE (b), BC-900/GCE (c), and Fe-BC-900/GCE (d) in N_2-saturated 0.1 mM H_2O_2 0.1 M KOH.

Figure 4B shows the CV curves of different modified electrodes containing 0.1 mM H_2O_2 N_2 saturated with 0.1 M KOH solution. As can be seen from the figure, no obvious reduction peaks were found for Fe-BC-300/GCE and Fe-BC-600/GCE, which is due to the low pyrolysis temperature and low graphitization, resulting in poor conductivity of the materials, making Fe-BC-300/GCE and Fe-BC-600/GCE very small in response to H_2O_2 current. bc-900/GCE has a −0.2 V BC-900/GCE has an insignificant reduction peak at −0.2 V. Most of the electrocatalytic effect of BC-900/GCE comes from the nitrogen and sulfur atoms doped in the carbon skeleton. Compared with other modified electrodes, Fe-BC-900/GCE has a larger current response to H_2O_2 and a lower H_2O_2 reduction potential, which inferred that Fe is the active center for H_2O_2 reduction in the material. The reduction process is a typical electrocatalytic process: Fe_{III} is reduced to Fe_{II}, H_2O_2 oxidizes Fe_{II} to Fe_{III}, and H_2O_2 is reduced to water in the reduction process [5]. Pig blood has a certain amount of Fe, which can be used as a catalytic reduction center for H_2O_2. The nanopore structure improves the contact efficiency between the catalytic center and H_2O_2, which improves the sensing performance of Fe-BC-900/GCE. The CVs of Fe-BC-900 in KOH solution with different pH value (12.3–13.3) was depicted in Figure S2. The Fe-BC-900/GCE has a good response in solutions of different pH values and peak current changes <10%, indicating a good pH tolerance.

The kinetics of H_2O_2 on the surface of Fe-BC-900/GCE was investigated by adjusting the sweep rate. Figure 5A shows the CV curves of Fe-BC-900/GCE in the sweep rate range of 40–200 mV s^{-1} in 0.1 M KOH buffer solution under N_2 saturation. It can be clearly observed from the figure that the current keeps increasing with the increasing scan rate. After calculation, the current is linearly related to the scan rate, and the fitted curve is shown in Figure 5B, with the linear relationship log I_{pc} (μA) = 0.575 log v (mV s^{-1}) + 0.515, where I_{pc} is the peak-current. This proves that the H_2O_2 reduction process on the Fe-BC-900/GCE surface is a surface-controlled process [7]. As shown in Figure 5 logI_{pc} and log$v$ are linearly related. The slope of 0.575 is obtained after the fit, which is higher than the value of 0.5 for the complete spreading control process and smaller than that of 1 for the complete adsorption control process, which indicates that the H_2O_2 molecules on the Fe-BC-900/GCE surface are subject to the spreading control process and the adsorption control process and is a preference for diffusion control [7].

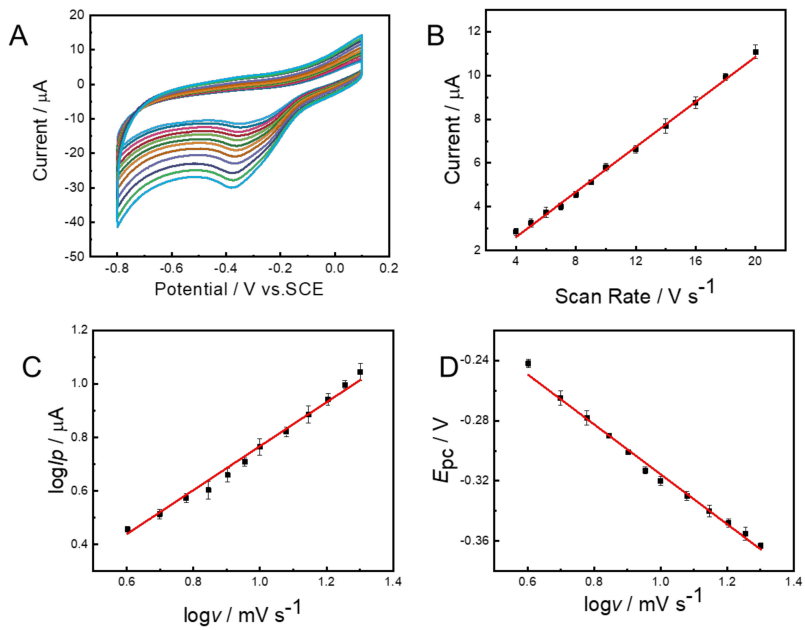

Figure 5. (**A**) CVs of the Fe-BC-900/GCE at different scan rates (40 to 200 mVs^{-1}) in 0.1 M. KOH containing 0.1 mM H_2O_2; (**B**) the dependence of reduction current on scan rate; (**C**) the relationship between log*I*p and log*v*; (**D**) the relationship between *I*pc and log*v*.

The Fe-BC-900/GCE kinetics were further investigated. As the scan rate increases, the relationship between Ep and logv is shown in Figure 5D, and the fitted curve can be expressed as $Ep = -0.138 \log v$ (mV s^{-1}) $- 0.147$.

For an irreversible electrode process, Epc can be defined by the following equation [38]

$$E_{pc} = E' - \frac{2.303RT}{anF} \log \frac{RTK}{anF} - \frac{2.303RT}{anF} \log v$$

where α is the transfer coefficient, which is usually assumed to be 0.5 in a totally irreversible electrode process [39], v is the scan rate, and n is the number of electrons transferred in the rate-determining step. Other symbols have their usual meanings. Accordingly, n is calculated to be 0.73. Thus, one electron is considered involved in the rate-determining step of H_2O_2 reduction.

The electrochemical sensing performance of Fe-BC-900/GCE for H_2O_2 was investigated using the amperometric method. Figure 6A,B show the chrono current curves for different H_2O_2 concentrations in Fe-BC-900/GCE in 0.1 M KOH buffer solution under N_2 saturation. It can be clearly seen from the figures that the reduction current increases rapidly with the addition of H_2O_2 and reaches a steady state within 3 s on average. Fe-BC-900 has a high degree of graphitization, which enhances the electron transfer rate between Fe-BC-900 and the electrode and therefore shortens the response time of the sensor to H_2O_2. Figure 6C shows the relationship between H_2O_2 concentration and current, and after fitting, the current and H_2O_2 concentration show a good linear relationship in the range of 0.1–2000 μM, R^2 = 0.9998, and the linear relationship equation is I_{pc} (μA) 1.052 + 0.03277c (μM) The detection limit is 0.046 μM. The experimental results show that Fe-BC-900/GCE can be applied to the quantitative detection of H_2O_2. As shown in Table 1, Fe-BC-900/GCE demonstrates better performance xompared with other H_2O_2 sensors reported before. Analysis of these two increasing waves by means of a standard addition plot against H_2O_2 concentration is shown in Figure 4B and Figure S4. It is shown that the standard addition plot is like that of the calibration curve, verifying the suitability of the procedures.

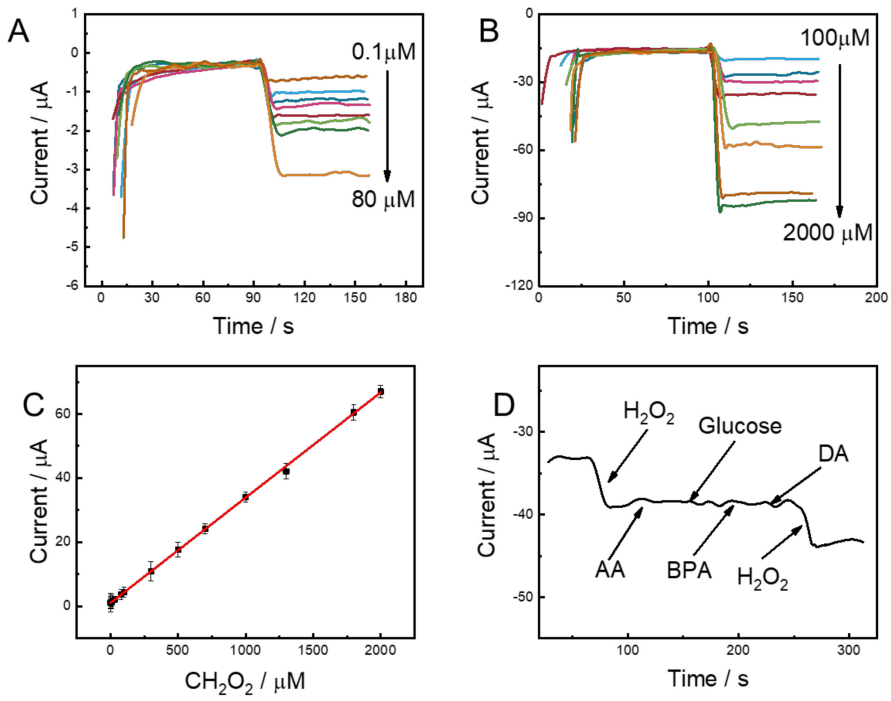

Figure 6. (**A**,**B**) Amperometric response of PPY-H-BNG/GCE upon the successive addition of H_2O_2 at low concentrations (from 0.1 to 2000 μM) into gently stirred 0.1 M KOH; (**C**) calibration curve of the Fe-BC-900/GCE as a function of H_2O_2 concentration; (**D**) amperometric response of Fe-BC-900/GCE exposed to 0.5 mM H_2O_2, 0.5 mM AA, 0.5 mM glucose, 0.1 mM BPA, 0.5 mM DA, and 0.5 mM H_2O_2.

Table 1. Comparison with previous literature.

Signal Amplification Strategy	Assay Principle	Linear Range μM	Limit of Detection μM	Reference
[a] Cu(bmtc)2(H_2O)]/SPCE	*i-t*	10–524	0.57	[40]
Cu microelectrode	*i-t*	15–1820	2.7	[41]
Nanoporous gold film electrode	*i-t*	1–1000	3.7	[42]
Porous Au film electrode	*i-t*	30–360	3	[43]
Nanoporous gold	*i-t*	10–1800	0.6	[44]
Fe-BC	*i-t*	0.1–2000	0.046	This work

[a] screen-printed carbon electrode (SPCE) modified with copper (II) 1-(3-bromobenzyl)-5-methyl-1H-1,2,3-triazole-4-carboxylate [Cu(bmtc)2(H_2O)].

To investigate the effect of coexisting interferents on the performance of Fe-BC-900/GCE, the Fe-BC-900/GCE interference testing experiment was investigated by adding ascorbic acid (AA), glucose, bisphenol A (BPA), and dopamine (DA). After adding 0.5 mM AA, glucose, BPA, and DA interferents sequentially, the current did not fluctuate significantly. Continuing to add 0.5 mM H_2O_2, the Fe-BC-900/GCE response had a significant current response with the first addition. This indicates that the added interferents have almost no effect on the reduction of the H_2O_2 Fe-BC-900 electrode surface, indicating that Fe-BC-900/GCE has excellent anti-interference properties. The stability of Fe-BC-900/GCE was investigated by continuous scanning CV cycles (Figure S3). After 100 cycle scans, there was no significant change in the CV curves before and after the comparison cycle, and the current response change was only 5%, which indicates that the H_2O_2 measurement has high stability, and therefore, Fe-BC-900 is an ideal material for constructing electrochemical sensors.

3. Materials and Methods

3.1. Materials

All reagents were analytically pure without further purification. Ethanol was purchased from Aladdin Chemistry Co., Ltd. (Shanghai, China).

Pig blood was collected at the Zibo central slaughterhouse. The pigs were about 3–4 years old. Scanning electron microscopy (SEM, FEI Co., Ltd., Hillsboro, OR, USA) was used to study the morphology of the modified electrode on an FEI SIRION microscope. Transmission electron microscope (TEM, FEI Co., Ltd., Hillsboro, OR, USA) images were obtained on an FEI Tecnai G2T20 at 200 kV. The synthesized samples were also analyzed using an X-ray photoelectron spectrometer (XPS) (K-Alpha, Waltham, MA, USA. Thermo Scientific). Raman spectra were used to analyze graphitic ordering by a LabRAM HR800 from JY Horiba.

Voltammetry tests were carried out on a CHI660E electrochemical system (CH Instrument, Shanghai, China) with a three-electrode system. A saturated calomel electrode (SCE) and a platinum foil electrode were used as a reference and auxiliary electrodes, respectively. The working electrode was prepared as follows: 5 mg catalyst was ultrasonically dispersed in 1 mL of DMF for 30 min, and then 5 μL of the mixture was dropped on a glassy carbon electrode (3 mm), followed by the evaporation in air.

3.2. Methods

Fresh pig blood (100 mL) was stirred thoroughly with an equal volume of distilled water and then placed in a constant temperature water bath (100 °C) and boiled until the proteins in the pig blood coagulated into clumps. The clotted pig blood was cooled at room temperature and freeze-dried afterward. Then, 2 g of pig-blood powder was weighed into a tube furnace and programmed to increase the temperature with a heating rate to 900 °C for 2 h, and the finished pig-blood powder was ground thoroughly and labeled as Fe-BC-900. As a control experiment, the composites were heated to 300 °C and 600 °C using the same procedure, and the materials were labeled as Fe-BC-300 and Fe-BC-600,

respectively. The prepared Fe-BC-900 was immersed in 0.1 M HCl for 12 h and repeatedly washed with secondary water and ethanol three times to prepare BC-900.

4. Conclusions

In this work, a novel strategy for constructing H_2O_2 electrochemical sensors using pig-blood biomass carbon materials is proposed for the first time. Fe-BC-900 nanomaterials were obtained by pyrolysis of fresh pig blood, and the novel nanomaterials have excellent electrocatalytic activity for H_2O_2, enabling direct detection of H_2O_2. The Fe-BC-900/GCE exhibits a wider detection concentration range of 0.1–2000 μM, a low LOD of 0.046 μM towards H_2O_2 detection, and excellent anti-interference performance. The excellent H_2O_2 electrocatalytic activity of Fe-BC-900/GCE expands the application of biomass carbon materials in the field of electrochemical sensors.

Supplementary Materials: The following supporting information can be downloaded at: https://www.mdpi.com/article/10.3390/catal12111438/s1, Figure S1: (A)isotherms of nitrogen sorption and (B) the corresponding QSDFT pore size distributions determined by adsorption branch of nitrogen sorption isotherms; Figure S2: CVs of the Fe-BC-900/GCE in different concentrations of KOH solutions with N_2-saturated 0.1 mM H_2O_2; Figure S3: Plots of (A) current measured at +0.15 V against the concentration of H_2O_2, (B) peak current measured at +0.29 V against the concentration of H_2O_2; Figure S4: CVs of the Fe-BC-900/GCE in 0.1 M KOH with 0.1 mM H_2O_2 solution at the first cycle and the 100 cycles, respectively.

Author Contributions: G.L.: Conceptualization, Methodology, Investigation, Visualization, Data Curation, Writing—Original Draft; X.L.: Methodology, Visualization, Investigation, Writing—review & editing; Q.W., K.S., C.L. and H.W.: Visualization, Formal analysis; Z.L.: Data Curation; W.S. Resources, Funding acquisition; Y.C.: Supervision, Visualization, Writing—review & editing; F.W.: Writing—review & editing. All authors have read and agreed to the published version of the manuscript.

Funding: This work was supported by the National Natural Science Foundation of China (51502161, 51572127, and 21576138), the Natural Science Foundation of Shandong Province (ZR2014EMQ008).

Data Availability Statement: Not applicable.

Conflicts of Interest: The authors declare no conflict of interest.

References

1. Wang, Q.; Han, N.; Shen, Z.; Li, X.; Chen, Z.; Cao, Y.; Si, W.; Wang, F.; Ni, B.-J.; Thakur, V.K. MXene-based electrochemical (bio) sensors for sustainable applications: Roadmap for future advanced materials. *Nano Mater. Sci.* 2022; *in press*. [CrossRef]
2. Zhang, R.; Chen, W.J.B. Recent advances in graphene-based nanomaterials for fabricating electrochemical hydrogen peroxide sensors. *Bioelectronics* **2017**, *89*, 249–268. [CrossRef] [PubMed]
3. Li, M.; Wang, P.; Li, F.; Chu, Q.; Li, Y.; Dong, Y. An ultrasensitive sandwich-type electrochemical immunosensor based on the signal amplification strategy of mesoporous core-shell Pd@Pt nanoparticles/amino group functionalized graphene nanocomposite. *Biosens. Bioelectron.* **2017**, *87*, 752–759. [CrossRef] [PubMed]
4. Xie, F.; Cao, X.; Qu, F.; Asiri, A.M.; Sun, X. Cobalt nitride nanowire array as an efficient electrochemical sensor for glucose and H_2O_2 detection. *Sens. Actuators B Chem.* **2018**, *255*, 1254–1261. [CrossRef]
5. Cao, Y.; Qi, Y.; Meng, X.; Si, W.; Hao, Q.; Lei, W.; Li, J.; Cao, J.; Li, X.; Li, Q.; et al. Facile Preparation of Hemin/Polypyrrole/N, B-Co-Doped Graphene Nanocomposites for Non-Enzymatic H_2O_2 Determination. *J. Electrochem. Soc.* **2018**, *165*, B623. [CrossRef]
6. Qi, X.; Yang, T.; Li, P.; Wei, Z. DFT study on ORR catalyzed by bimetallic Pt-skin metals over substrates of Ir, Pd and Au. *Nano Mater. Sci.* 2021; *in press*. [CrossRef]
7. Cao, Y.; Si, W.; Hao, Q.; Li, Z.; Lei, W.; Xia, X.; Li, J.; Wang, F.; Liu, Y. One-pot fabrication of Hemin-NC composite with enhanced electrocatalysis and application to H_2O_2 sensing. *Electrochim. Acta* **2018**, *261*, 206–213. [CrossRef]
8. Cao, Y.; Zhang, W.; Sun, Y.; Jiang, Y.; Han, N.; Zou, J.; Si, W.; Wang, F.; Núñez-Delgado, A.; Liu, S. Highly active iron-nitrogen-boron-carbon bifunctional electrocatalytic platform for hydrogen peroxide sensing and oxygen reduction. *Environ. Res.* **2021**, *201*, 111563. [CrossRef]
9. Wang, J.; Zhao, C.-X.; Liu, J.-N.; Ren, D.; Li, B.-Q.; Huang, J.-Q.; Zhang, Q. Quantitative kinetic analysis on oxygen reduction reaction: A perspective. *Nano Mater. Sci.* **2021**, *3*, 313–318. [CrossRef]
10. Sun, Y.; Zhang, W.; Wang, Q.; Han, N.; Núñez-Delgado, A.; Cao, Y.; Si, W.; Wang, F.; Liu, S. Biomass-derived N, S co-doped 3D multichannel carbon supported Au@ Pd@ Pt catalysts for oxygen reduction. *Environ. Res.* **2021**, *202*, 111684. [CrossRef]

11. Gao, Z.; Zhang, Y.; Song, N.; Li, X. Biomass-derived renewable carbon materials for electrochemical energy storage. *Mater. Res. Lett.* **2017**, *5*, 69–88. [CrossRef]
12. Duran-Jimenez, G.; Monti, T.; Titman, J.; Hernandez-Montoya, V.; Kingman, S.; Binner, E. New insights into microwave pyrolysis of biomass: Preparation of carbon-based products from pecan nutshells and their application in wastewater treatment. *J. Anal. Appl. Pyrolysis* **2017**, *124*, 113–121. [CrossRef]
13. Zhao, L.; Jiang, J.; Xiao, S.; Li, Z.; Wang, J.; Wei, X.; Kong, Q.; Chen, J.S.; Wu, R. PtZn nanoparticles supported on porous nitrogen-doped carbon nanofibers as highly stable electrocatalysts for oxygen reduction reaction. *Nano Mater. Sci.* 2022; *in press*. [CrossRef]
14. Qin, D.; Chen, S. A sustainable synthesis of biomass carbon sheets as excellent performance sodium ion batteries anode. *J. Solid State Electrochem.* **2017**, *21*, 1305–1312. [CrossRef]
15. Tian, N.; Qin, A.M.; Liao, L.; Zhang, K.Y.; Wang, M.P. Synthesis of MoSe2-MoO2@ Biomass-Derived Honeycombed Carbon Composite and Its Application in LIB. In *Key Engineering Materials*; Trans Tech Publications, Ltd.: Bäch, Switzerland, 2017; Volume 727, pp. 645–652. [CrossRef]
16. Liu, M.; Yin, X.; Guo, X.; Hu, L.; Yuan, H.; Wang, G.; Wang, F.; Chen, L.; Zhang, L.; Yu, F. High efficient oxygen reduction performance of Fe/Fe3C nanoparticles in situ encapsulated in nitrogen-doped carbon via a novel microwave-assisted carbon bath method. *Nano Mater. Sci.* **2019**, *1*, 131–136. [CrossRef]
17. Gong, Y.; Li, D.; Luo, C.; Fu, Q.; Pan, C. Highly porous graphitic biomass carbon as advanced electrode materials for supercapacitors. *Green Chem.* **2017**, *19*, 4132–4140. [CrossRef]
18. Deng, L.; Zhong, W.; Wang, J.; Zhang, P.; Fang, H.; Yao, L.; Liu, X.; Ren, X.; Li, Y. The enhancement of electrochemical capacitance of biomass-carbon by pyrolysis of extracted nanofibers. *Electrochim. Acta* **2017**, *228*, 398–406. [CrossRef]
19. Ouyang, J. Applications of carbon nanotubes and graphene for third-generation solar cells and fuel cells. *Nano Mater. Sci.* **2019**, *1*, 77–90. [CrossRef]
20. Wang, H.; Fu, F.; Huang, M.; Feng, Y.; Han, D.; Xi, Y.; Xiong, W.; Yang, D.; Niu, L. Lignin-based materials for electrochemical energy storage devices. *Nano Mater. Sci.* 2022; *in press*. [CrossRef]
21. Pistone, A.; Espro, C. Current trends on turning biomass wastes into carbon materials for electrochemical sensing and rechargeable battery applications. *Curr. Opin. Green Sustain. Chem.* **2020**, *26*, 100374. [CrossRef]
22. Yu, Z.; Liu, C.; Chen, J.; Yuan, Z.; Chen, Y.; Wei, L. High-performance Fe–N–C electrocatalysts with a "chain mail" protective shield. *Nano Mater. Sci.* **2021**, *3*, 420–428. [CrossRef]
23. Mao, S.; Wang, Z.; Chen, Z.; Wu, K.; Zhang, K.; Li, Q.; Yan, H.; Lü, G.; Huang, G.; Wang, Y. Towards the selectivity distinction of phenol hydrogenation on noble metal catalysts. *Nano Mater. Sci.* 2020; *in press*. [CrossRef]
24. Bhat, V.S.; Supriya, S.; Hegde, G. Biomass derived carbon materials for electrochemical sensors. *J. Electrochem. Soc.* **2019**, *167*, 037526. [CrossRef]
25. Li, C.; Luo, M.; Xia, Z.; Guo, S. High-index faceted noble metal nanostructures drive renewable energy electrocatalysis. *Nano Mater. Sci.* **2020**, *2*, 309–315. [CrossRef]
26. Zhang, Z.; Chen, K.; Zhao, Q.; Huang, M.; Ouyang, X. Electrocatalytic and photocatalytic performance of noble metal doped monolayer MoS_2 in the hydrogen evolution reaction: A first principles study. *Nano Mater. Sci.* **2021**, *3*, 89–94. [CrossRef]
27. Chen, M.; Jiang, S.; Huang, C.; Wang, X.; Cai, S.; Xiang, K.; Zhang, Y.; Xue, J. Honeycomb-like Nitrogen and Sulfur Dual-Doped Hierarchical Porous Biomass-Derived Carbon for Lithium–Sulfur Batteries. *ChemSusChem* **2017**, *10*, 1803–1812. [CrossRef]
28. Yang, H.; Tang, Y.; Sun, X.; Liu, Q.; Huang, X.; Wang, L.; Fu, Z.; Zhang, Q.; Or, S.W. Biomass-derived porous carbon materials with NiS nanoparticles for high performance supercapacitors. *J. Mater. Sci. Mater. Electron.* **2017**, *28*, 14874–14883. [CrossRef]
29. Gao, S.; Li, X.; Li, L.; Wei, X. A versatile biomass derived carbon material for oxygen reduction reaction, supercapacitors and oil/water separation. *Nano Energy* **2017**, *33*, 334–342. [CrossRef]
30. Yang, W.; Xu, S.; Ma, K.; Wu, C.; Gates, I.D.; Ding, X.; Meng, W.; Gao, Z. Geometric structures, electronic characteristics, stabilities, catalytic activities, and descriptors of graphene-based single-atom catalysts. *Nano Mater. Sci.* **2020**, *2*, 120–131. [CrossRef]
31. De Clercq, R.; Dusselier, M.; Sels, B.F. Heterogeneous catalysis for bio-based polyester monomers from cellulosic biomass: Advances, challenges and prospects. *Green Chem.* **2017**, *19*, 5012–5040. [CrossRef]
32. Zhao, X.; Pang, J.; Li, G.; Liu, F.; Xu, J.; Zheng, M.; Li, N.; Li, C.; Wang, A.; Zhang, T. Activated Carbon and Ordered Mesoporous Carbon-Based Catalysts for Biomass Conversion. In *Nanoporous Catalysts for Biomass Conversion*; Wiley and Sons: Hoboken, NJ, USA, 2017; pp. 17–54. [CrossRef]
33. Jia, Z.; Li, Z.; Ni, T.; Li, S. Adsorption of low-cost absorption materials based on biomass (*Cortaderia selloana* flower spikes) for dye removal: Kinetics, isotherms and thermodynamic studies. *J. Mol. Liq.* **2017**, *229*, 285–292. [CrossRef]
34. Han, N.; Zhao, X.; Thakur, V.K. Adjusting the interfacial adhesion via surface modification to prepare high-performance fibers. *Nano Mater. Sci.* **2021**, *in press*. [CrossRef]
35. Veeramani, V.; Sivakumar, M.; Chen, S.-M.; Madhu, R.; Alamri, H.R.; Alothman, Z.A.; Hossain, S.A.; Chen, C.-K.; Yamauchi, Y.; Miyamoto, N.; et al. Lignocellulosic biomass-derived, graphene sheet-like porous activated carbon for electrochemical supercapacitor and catechin sensing. *RSC Adv.* **2017**, *7*, 45668–45675. [CrossRef]
36. Wu, Z.; Yang, W.; Chen, L.; Meng, H.; Zhao, J.; Wang, S. Morphology and microstructure of co-pyrolysis char from bituminous coal blended with lignocellulosic biomass: Effects of cellulose, hemicellulose and lignin. *Appl. Therm. Eng.* **2017**, *116*, 24–32. [CrossRef]

37. Chulliyote, R.; Hareendrakrishnakumar, H.; Raja, M.; Gladis, J.M.; Stephan, A.M. Sulfur-Immobilized Nitrogen and Oxygen Co–Doped Hierarchically Porous Biomass Carbon for Lithium-Sulfur Batteries: Influence of Sulfur Content and Distribution on Its Performance. *ChemistrySelect* **2017**, *2*, 10484–10495. [CrossRef]
38. Watanabe, M.; Uchida, M.; Motoo, S. Preparation of highly dispersed Pt+ Ru alloy clusters and the activity for the electrooxidation of methanol. *J. Electroanal. Chem. Interfacial Electrochem.* **1987**, *229*, 395–406. [CrossRef]
39. Si, W.; Han, Z.; Lei, W.; Wu, Q.; Zhang, Y.; Xia, M.; Hao, Q. Fast electrochemical determination of imidacloprid at an activated glassy carbon electrode. *J. Electrochem. Soc.* **2013**, *161*, B9. [CrossRef]
40. Quezada, V.; Martinez, T.; Nelson, R.; Pérez-Fehrmann, M.; Zaragoza, G.; Vizcarra, A.; Kesternich, V.; Hernández-Saravia, L.P. A novel platform of using copper (II) complex with triazole-carboxilated modified as bidentated ligand SPCE for the detection of hydrogen peroxide in milk. *J. Electroanal. Chem.* **2020**, *879*, 114763. [CrossRef]
41. Dantas, L.M.F.; Castro, P.S.; Peña, R.C.; Bertotti, M. Amperometric determination of hydrogen peroxide using a copper microelectrode. *Anal. Methods* **2014**, *6*, 2112–2116. [CrossRef]
42. Sukeri, A.; Lima, A.S.; Bertotti, M. Development of non-enzymatic and highly selective hydrogen peroxide sensor based on nanoporous gold prepared by a simple unusual electrochemical approach. *Microchem. J.* **2017**, *133*, 149–154. [CrossRef]
43. Sukeri, A.; Bertotti, M. Electrodeposited honeycomb-like dendritic porous gold surface: An efficient platform for enzyme-free hydrogen peroxide sensor at low overpotential. *J. Electroanal. Chem.* **2017**, *805*, 18–23. [CrossRef]
44. Arjunan, A.; Sukeri, A.; Saraiva, D.P.M.; Miranda, P.B.; Bertotti, M. Electrochemical studies of hydrogen peroxide oxidation on a nanoporous gold surface: Fundamental and analytical applications. *J. Electrochem. Soc.* **2020**, *167*, 116507. [CrossRef]